Wireless Power Transfer to Biomedical Implants Using a Class-E Inverter and a Class-DE Rectifier

Wireless Power Transfer to Biomedical Implants Using a Class-E Inverter and a Class-DE Rectifier

Tom P. G. van Nunen, *Student Member, IEEE*, Rob M. C. Mestrom, *Member, IEEE*, and Hubregt J. Visser, *Senior Member, IEEE*

***Abstract*—In this article, we propose a strategy for the design of a wireless power transfer system consisting of a class-E inverter, a half-bridge class-DE rectifier, and two coupled coils. The system is optimized for maximum power transfer efficiency. The design is validated via a case study, for which a wireless power transfer link to a neuroprosthesis was designed. After circuit simulations, a prototype was realized and measured. There is a good agreement between the calculated, simulated and measured voltages and currents. The prototype delivers 80 mW, 7 V to a biomedical implant at 6.78 MHz, the transfer efficiency is 52 to 68%, depending on the alignment. The end-to-end efficiency, with the controller and gate driver also taken into account, is 39 to 57%. Electromagnetic and thermal simulations were performed to verify compliance with relevant safety regulations on specific absorption rate (SAR) levels, magnetic field strength, and heat generation in the implant, for separation distances between the coils of 8 to 15 mm, and transverse misalignment from 0 to 15 mm.**

***Index Terms*—Wireless power transfer, implantable medical device, bioelectronics, class-E inverter, class-DE rectifier.**

I. Introduction

GLOBALLY, over 43 million people are blind, and this number is expected to reach 61 million by the year 2050 [1]. In more than 90% of the cases, blindness is caused by disease, accident, and/or aging, rather than being congenital. Functional vision could one day be restored using a neuroprosthesis [2], which is the goal of the NESTOR project [3]. The neuroprosthesis will consist of an implantable medical device (IMD) which is connected to 1024 electrodes, implanted in the visual cortex. When stimulated, each electrode will elicit a 'phosphene', i.e. the perception of a dot of light. Stimulating multiple electrodes simultaneously may enable to the perception of shapes, and successive stimulation to the perception of motion [2]. Ultimately, this visual prosthesis intends to restore (rudimentary) functional vision in blind people.

Wires penetrating the skin can cause serious infection, and are thus to be avoided in (semi-)permanent IMDs. For many applications, including this one, adding a battery is undesired, due to the physical size increase of the IMD. Therefore, the IMD will be powered wirelessly.

Much progress has been made in the field of inductive wireless power transfer (WPT) in recent years and impressive results have been achieved [4], [5], [6], [7]. Related work is not directly applicable to our situation, because in some cases the validation is performed in air rather than in a representative environment [8], [9], specific absorption rate (SAR) simulations or measurements are not performed [8], [9], [10], [11], [12], [13], [14], the reported power transfer efficiency (PTE) does not include the transmit and receive electronics [11], [15], [16], the used frequency band is not allowed for WPT in Europe [8], [12], [16], [17], [18], or the heat generation in the IMD is too high [19], [20], [21]. This work presents the design and validation of a biomedical WPT prototype, which can transfer up to 170 mW with ideal alignment. It can transfer over 80 mW when the misalignment between the coils is below 15 mm, and the separation distance between the coils is between 8 and 15 mm. The system operates at 6.78 MHz, and is designed to achieve maximum power transfer efficiency (MPTE). The prototype is validated in a realistic environment, simulations show compliance with the relevant SAR regulations [13], [14], field strength regulations [18], and thermal regulations [20], [21].

II. Design Requirements

The implanted electrodes have an impedance of 50 k Ω [22] and require a bipolar current with a maximum amplitude of $50\,\mu$ A to produce a phosphene. This corresponds to a symmetrical power supply voltage of ± 2.5 V. A headroom of 1 V is added to each power supply rail to cover the voltage drop over the amplifiers, resulting in a required voltage at the receiver of ± 3.5 V, or 7 V in total. The waveform for each electrode is $200\,\mu$s positive, $200\,\mu$s negative, and has a period of 3 ms. The efficiency of the amplifiers is assumed to be better than 50% [23]. When we assume simultaneous activation of at most 20% of the 1024 electrodes at any given time is sufficient to produce a useful image in the patient, the maximum power consumption of the stimulation electronics is 2.4 mW.

The downlink receiver consumes 1 mW, and the uplink transmitter consumes $3-15$ mW, depending on the data rate [24]. The power required for neural recording, (un)packing the data and controlling the implant is still being researched, but from related work [23], [25], the total power required for the recording

Manuscript received 4 October 2022; revised 4 February 2023; accepted 5 April 2023. Date of publication 1 May 2023; date of current version 23 August 2023. This work was supported by the Dutch Technology Foundation STW, which is part of the Netherlands Organization for Scientific Research (NWO), Project 5 of the NESTOR program (P15-42). *(Corresponding author: Hubregt J. Visser.)*

The authors are with the Department of Electrical Engineering, Eindhoven Univerisity of Technology, 5600MB Eindhoven, The Netherlands (e-mail: t.p.g.v.nunen@tue.nl; r.m.c.mestrom@tue.nl; h.j.visser@tue.nl).

This article has supplementary downloadable material available at https://doi.org/10.1109/JERM.2023.3267042, provided by the authors.

Digital Object Identifier 10.1109/JERM.2023.3267042

part is estimated to be $18-35$ mW, and the stimulation part is expected to consume a total of 15 mW. The brain implant is thus expected to consume up to 50 mW.

In this work, we design the WPT link to deliver 90 mW to the load, such that we have the possibility to increase the number of electrodes in the future, or change them for types with a lower impedance, without having to redesign the entire WPT link. At $V_{out} = 7$ V, this corresponds to $R_L = 544.4\,\Omega$. The inverter will be powered with $V_{dc} = 5$ V, which is directly available from a standard USB port.

III. Coil Design

The design process starts with the selection of the coils. Pinuela et al. [26] describe an approach for maximizing the end-to-end efficiency of a WPT system with a class-E inverter. In particular, they state that, for achieving MPTE, the coils should be as large as possible, have as many turns as possible, and have a wire diameter as large as possible. However, part of their optimization relies on choosing an optimal frequency, whereas the permitted range of operating frequencies in real applications is often severely limited [18].

A. Coil Size

Available space for a subcutaneous receiver (Rx) coil is limited. Consultations with a neurosurgeon made us decide for an Rx coil diameter below 40 mm and a thickness (including biocompatible coating) below 3 mm. Increasing the diameter or adding turns will improve k. Although this will also increase the equivalent series resistance (ESR) and lower the self-resonance frequency (SRF), we found that the increase in k outweighs the increase in ESR. The Rx coil should thus have as much turns as possible with as thick wire as possible, without exceeding the size constraints, and whilst making sure the SRF is at least twice the frequency of operation.

With software like FastHenry [27], inductances, ESRs and coupling factors can be calculated. With these values, the maximum achievable link efficiency - i.e. coils only - can be estimated [28]. Inverter and rectifier losses will be added later. FastHenry cannot calculate the coil's SRF, and the given ESR will be too low if the frequency of operation is close to the SRF. Furthermore, the influence of the surrounding biological tissue is not taken into account.

Multiple Rx coils with a diameter of 35 mm were manufactured, with a wire thickness of 0.25 and 0.6 mm, having 3 to 10 turns, sealed in a $2 \times 125\,\mu$m thick PET pouch, and their properties measured in a 0.9% (0.154 M) saline solution [29]. The Rx coil with 7 turns of 0.25 mm wire yields the highest maximum achievable efficiency. Copper wire cannot be used in the final product, as copper is a neurotoxin. A 0.25 mm diameter copper (Cu) wire corresponds to a 0.30 mm diameter gold (Au) wire, which can be used safely, but is not used in this prototype for economical reasons.

The transmitter (Tx) coil should be large enough to allow for a radial misalignment d of up to 15 mm. With the aid of FastHenry [27], it was found that a flat coil with an inner diameter of 35 mm is sufficient. A thicker wire than in the Rx coil is used, as this reduces the losses, and there is no need for this coil to be flexible. Using too thick a wire can result in a bulky coil. A wire diameter of 1.0 mm was chosen. The number of turns should be as large as possible [26], whilst the SRF is high enough. A flat Tx coil of 10 turns was chosen, resulting in an outer diameter of 55 mm, which is considered acceptably small, while the measured ESR and SRF are acceptable.

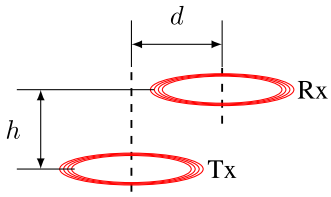

Fig. 1. Separation h and radial misalignment d between the coils.

The candidate coils were modeled in FastHenry. The Tx coil has an inductance of $6.9\,\mu$H with an ESR of $1.2\,\Omega$, whereas the measured values are $6.8\,\mu$H and $3.0\,\Omega$ (SRF 25.5 MHz). The increase in ESR is believed to be caused by the fact that the coil operates relatively close to its SRF, the effects of which FastHenry is unable to model accurately. The Rx coil has an inductance of $4.9\,\mu$H with an ESR of $2.9\,\Omega$, whereas the measured values are $4.5\,\mu$H and $3.5\,\Omega$ (SRF 18.5 MHz). The increase in ESR is caused by the measured coil being submerged in a 0.9% saline solution.

B. Coil Alignment

The normal thickness of the human scalp is 2 to 5 mm [30], [31], [32], although it can be thicker in the days after surgery. To prevent the risk of skin irritation, the Tx coil will not be placed directly on the skin. A comfortable headband with a thickness of 4 to 6 mm is assumed to hold the Tx unit. The enclosure of the Tx unit is chosen to be 2 mm thick, such that it can be 3D-printed easily. This means that the height h between the external Tx coil and implanted Rx coil is in the range from 8 to 15 mm.

The Tx unit will be mounted on a headband, which will be positioned by the patient. This introduces uncertainty in the exact location of the Tx coil relative to the Rx coil. Furthermore, the headband could move slightly over time. It is yet unclear what values can be expected for the radial misalignment, but for now we assume choosing the upper bound for the radial misalignment d at 15 mm will be sufficient. Fig. 1 shows the positioning of the two coils.

For different values of h and d, see Fig. 1, the mutual and self inductances M and L and the ESRs of the coils are measured, as shown in Fig. 2. Next, the expected maximum theoretical link efficiency η_{max} is calculated [28]. The link has to operate for $8 \leq h \leq 15$ mm and $0 \leq d \leq 15$ mm, which can be seen to correspond to a range for the coupling factor k of roughly $0.14 \leq k \leq 0.37$. The maximum theoretical link efficiency η_{max} is between 86 and 95%.

The value for η_{max} is an indicative upper bound only, and will not be met in practice, because losses in the inverter and rectifier are present. Furthermore, the load is assumed to be optimized for each value of k, whereas in practice, only a single value can

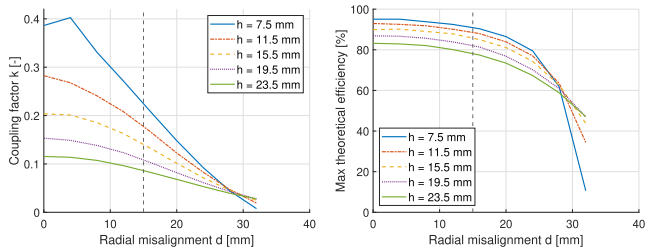

(a) Measured coupling factor. (b) Maximum theoretical efficiency.

Fig. 2. Measured coupling factor k and maximum theoretical link efficiency η_{max} for different combinations of separation distance d and radial misalignment h.

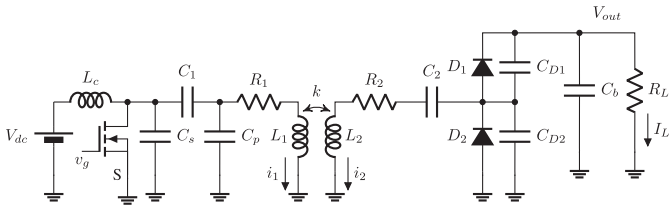

Fig. 3. Schematic of the WPT link, consisting of a class-E inverter (left) and a class-DE rectifier (right). The wireless coupling (k) occurs through coils L_1 and L_2.

be chosen[1], and all other cases will implicitly operate with a load that is (slightly) less optimal.

C. Coupling Factor

Even though the link will be optimized for a single value k_{opt}, it should be designed such that its performance is acceptable for the full range of k.

The initial guess for k_{opt} was 0.25, as this is in the middle of the required range. The results of the design process were simulated in LTspice [34], as will be explained in more detail in Section IV. It was found that the required output voltage of 7 V could not be reached for the required range of k, and therefore $k_{opt} = 0.25$ was rejected. After some iteration, the value $k_{opt} = 0.20$ was chosen, resulting in an output voltage above 7 V for the required range of k.

IV. Inverter and Rectifier Design

An inductive WPT system comprises an inverter, two or more coils, and a rectifier. Inverter and rectifier designs can be divided into various classes, each with certain characteristic properties, such as efficiency, susceptibility to load variations, required control signals, and part count. In biomedical WPT applications, as well as others, it is beneficial to have a small size, high efficiency, and limited design complexity. Therefore, the use of a system consisting of a class-E inverter and a class-DE rectifier is proposed [35]. The circuit of a typical class-E/DE WPT system is depicted in Fig. 3.

Kazimierczuk and Czarkowski [36] have presented a set of equations that can be used to design a class-E inverter. Fukui and Koizumi [37] have presented a set of equations that can be used to design a class-DE rectifier. Nagashima et al. [38] used both to design a WPT system consisting of a class-E inverter and a class-DE rectifier. However, the design process mentioned in [38] is not complete. Namely, the maximum efficiency is determined empirically, instead of analytically: a range of WPT systems is designed and simulated in a circuit simulator, each for a different value of the receiver diode duty cycle D_d, after which the solution that yields the highest efficiency is chosen. Secondly, the choice of the input voltage V_{dc} is not discussed. Furthermore, it is unclear how the behavior of the WPT system changes when the coupling factor k or the load R_L deviate from their optimal value.

For the design presented in this work, the input impedance of the rectifier Z_{in}, as seen from the Rx coil, is chosen such that the conditions for MPTE are satisfied [28] at $k = k_{opt}$. A class-DE rectifier has an input impedance of the form $Z_{in} = R_{in} + (\mathrm{j}\omega C_{in})^{-1}$ [37]. The duty cycle D_d of the diodes affects Z_{in}, and can thus be used to tune the input impedance to a desired value [38]. D_d should be chosen such that the resulting R_{in} is equal to the load resistance R'_L from [28] that achieves MPTE. The corresponding value for C_{in} is in series with C_2, which can be used to bring the receiver in resonance. This is the case when the imaginary parts of the impedances cancel eachother. The value for C_2 should thus be chosen such that

$$\mathrm{j}\omega L_2 + (\mathrm{j}\omega C_2)^{-1} + (\mathrm{j}\omega C_{in})^{-1} = 0. \tag{1}$$

The rest of the component values can be calculated according to [36], [37], [38]. Table I lists the resulting values.

TABLE I
Calculated and Simulated Component Values

Component	Calculated value [ref]	Simulated value
C_1	82.6 pF [36], [38]	82 pF
C_2	166.1 pF [28], [37], [38]	168 pF
C_p	17.0 pF [36], [38]	15 pF
C_s	61.8 pF [36], [38]	22 pF
$C_{D1,2}$	63.0 pF [28], [37], [38]	36 pF
L_C	71.7 μH [36], [38]	47 μH (SRF 15.8 MHz)

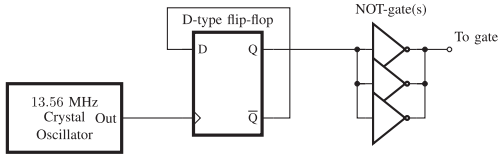

Fig. 4. 50% duty cycle 6.78 MHz oscillator and gate driver.

A. Controller

We choose to operate the switch of the inverter at a duty cycle of 50%, as this drive signal can be generated with just three basic components. The circuit in Fig. 4 shows a circuit that creates a 6.78 MHz gate drive signal with $D_s = 0.5$.

A crystal oscillator creates a 13.56 MHz signal. This signal toggles the output every period of the input signal, effectively halving the input frequency and creating a square wave with a 50% duty cycle. The output of the flip-flop is fed to 3 parallel

[1]It is possible to design a WPT system for coupling-independent operation, but this requires a variable frequency of operation [33], which is not desired in a medical application [18].

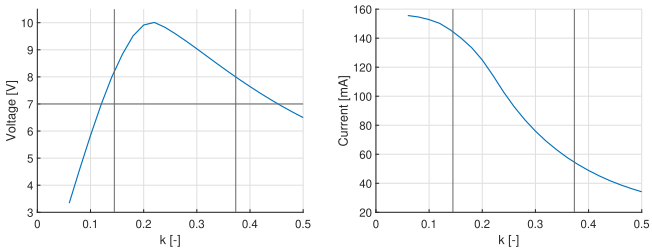

(a) Simulated DC output voltage. (b) Simulated Tx coil current.

Fig. 5. Simulated DC output voltage and Tx coil current as a function of k.

NOT-gates, that together can supply the current required to drive the gate of MOSFET S in the class-E inverter in Fig. 3.

It is possible to add extra safety features to the circuit, such as a current sensor that measures whether or not the input current I_{dc} is within predefined safety limits, or a temperature sensor. The output of such a sensor can be connected to the reset pin of the flip-flop (not shown), such that the gate voltage is zero when an unsafe condition is detected.

V. Prototype

The design was simulated in LTspice [34]. Table I lists the calculated component values, and the ones used in the circuit simulation. Three simulated values notably differ from their calculated value: C_s, $C_{D1,2}$, and L_c. C_s is smaller than calculated to compensate for the output capacitance of MOSFET S, which is in the same order of magnitude. L_c is smaller than calculated, because available parts with an inductance larger than $47\,\mu$H are not suitable, since their size is too large, their losses are too high, or their SRF is too low. The capacitance of the diodes $D_{1,2}$ is much lower than $C_{D1,2}$, so these do not need to be compensated for. However, from a sensitivity analysis, it was found that decreasing their value improves the efficiency and output voltage. Choosing 36 pF gives the optimal result.

The simulated output voltage is shown as a function of k in Fig. 5(a). At $k = k_{opt}$, the output voltage is 9.9 V, which corresponds to an output power of 180 mW. This is higher than designed, which is believed to be caused by the fact that the link operates at an input voltage $V_{dc} = 5.0$ V, being about 35% higher than the optimal value calculated in [37]. As a result, the simulated output voltage is about 42% higher than the output voltage for which the link was designed.

The advantage of this higher output voltage is that the required 7.0 V is achieved for a larger range of values for k, namely $0.12 \leq k \leq 0.45$, which includes the complete design range for k, as shown in Fig. 5(a).

The amplitude of the current through the Tx coil I_1, at $k_{opt} = 0.20$, is calculated to be 69 mA. As can be seen in Fig. 5(b), circuit simulations show it to be about 81% higher. This difference can be partly explained by the above-discussed voltage difference. Further, we expect that the assumptions on which the models are based [36], [37], [38], might not be completely valid anymore at the relative low power values that our WPT system operates on. For sure, the semiconductors will not operate as ideal switches.

TABLE II
Components Used in the Prototype

Component	Value	Part number
C_1	82 pF	251R14S820JV4T
C_2	168 pF	CBR06C680F5GAC
	(100 + 68)	06031A101JAT2A
C_p	15 pF	SQCSVA150JAT1A
C_s	22 pF	251R14S220JV4T
$C_{D1,2}$	36 pF	CBR06C360F5GAC
C_b	2×100 nF	GRM188R72A104KA35D
L_C	47 μH	DS1608C-473MLC
R_L	544.4 Ω	
S	GaN MOSFET	GS-065-004-1-L
$D_{1,2}$	Schottky	BAS40-04
Oscillator	13.56 MHz	X1G004451007312
Flip-flop	D-type	NC7SZ74K8X
NOT-gate	Triple	74LVC3G14DC,125
Voltage regulator	3.3 V	MIC5504-3.3YM5-TR
Decoupling capacitor	100 nF	GRM188R72A104KA35D
Decoupling capacitor	1 μF	GCM188R71C105KA64D

Fig. 6. Realized transmitter (left) and receiver (right) prototypes. Standard 2×1 LEGO brick for size.

A. Selection of Parts

MOSFETS and diodes have parasitic capacitances, which add to the capacitors that are connected parallel to them. The MOSFET and diodes should be chosen such that their parasitic capacitances are (well) below the values of C_s and $C_{D1,2}$, respectively. For the diode, a Schottky diode with $C_j < 3.6$ pF was chosen, and the MOSFET has $C_{oss} < 50$ pF. As these values are voltage dependent, it requires some fine tuning in LTspice to find the optimal value for C_s and $C_{D1,2}$. Table II shows the components used in the final prototype, rounded to the nearest commercially available value, based on a sensitivity analysis (not shown). The capacitors have a tolerance of $\pm 5\%$ or better. The oscillator and each of the chips have a decoupling capacitor connected at the power pins.

The prototype should preferably be as small as possible, yet the components should not be too small, as they will be soldered by hand. Therefore, SMD capacitors with a 0603 form factor were used, and chips with a pitch over 0.5 mm.

Components such as capacitors and inductors are not ideal in practice. They are chosen such that their self-resonance frequency is at least twice the operating frequency. Furthermore, they are chosen to have an ESR as low as possible, and a Q-factor as high as possible.

Fig. 6 shows the finished prototype. A detailed analysis of the performance under different load conditions is presented in the next section. The total printed circuit board (PCB) area of the

TABLE III
THERMAL AND DIELECTRIC TISSUE PROPERTIES AT 6.78 MHZ [39], [40]

Parameter	Scalp	Skull	CSF	Grey matter
Relative permittivity ε_r	478	47.6	109	397
Conductivity σ [S/m]	0.147	0.0392	2.00	0.252
Mass density ρ [kg/m^3]	1010	1810	1007	1039
Specific heat C [J/kgK]	3500	1300	4096	3680
Thermal conductivity K [W/mK]	0.420	0.300	0.57	0.565
Blood perfusion B [W/m^{3}K]	9100	1000	0	35000
Metabolic rate A_0 [W/m^3]	1000	0	0	10000

inverter prototype measures $21.0 \times 16.0 = 336$ mm^2, including a micro-USB connector for power. The rectifier measures $7.4 \times 6.4 = 47.4$ mm^2. The combined cost of the components, excluding the PCB and Tx and Rx coils, is less than € 10,- in bulk manufacture.

B. Safety Limits

A biomedical implant should meet several exposure limits before it can be considered safe. In particular, tissue should not heat up too much as a result of generated electromagnetic (EM) fields [13], [14] and heat generation in the implant [20], [21], and the transmitted magnetic fields should stay below a certain limit at a distance [18].

1) Tissue Heating by EM Fields: When EM fields interact with biological tissue, energy is absorbed in the tissue, which consequently heats up. The SAR of the tissue can be calculated by averaging $\frac{1}{2}\sigma|\vec{E}|^2$ over a defined mass. According to [13], [14], the SAR limit for continuous local exposure of the human head is 2 W/kg, to be averaged over a 10 g cubic volume.

The coils were simulated in Simulia CST Studio Suite, using the dielectric properties of Table III [39] for the human tissues involved. The Rx coil is assumed to be flat. The Tx coil current amplitude was obtained through the LTspice simulation described earlier and depends on the distance h and misalignment d between the coils, as can be deduced from Figs. 2(a) and 5(b). The corresponding SAR was obtained for a planarly layered model with a scalp thickness of 2 to 4 mm, a skull thickness of 6.5 mm, and a cerebro-spinal fluid (CSF) thickness of 3.2 mm [30], [31], [32]. The worst-case SAR occurs when the scalp thickness is 2 mm. A total of 40 simulations were performed, for $8 \leq h \leq 15$ and $0 \leq d \leq 16$ mm.

The simulated SAR is between 0.38 and 0.58 W/kg. Hence, the designed WPT link complies with the standard for the complete range of h and d, with a fair margin.

2) Magnetic Field Limits: A WPT link operating at 6.78 MHz should not generate magnetic fields are stronger than 42 dBμA/m at a distance of 10 m, according to ETSI EN 303 417 [18]. The Tx coil was simulated in Simulia CST Studio Suite, driven by a current of 150 mA. The simulation volume is $2 \times 2 \times 2$ m.

The simulated magnetic field strength at 10 cm is 117.7 dBμA/m, and at 1 m it is 58.6 dBμA/m, a difference of almost 60 dB. According to the Biot-Savart law, the magnetic field on the axis of a circular loop decays with r^3, which corresponds to the 60 dB difference mentioned above. The field at 10 m would thus be -1.4 dBμA/m, hence the prototype complies with ETSI EN 303 417 [18], even in the worst case.

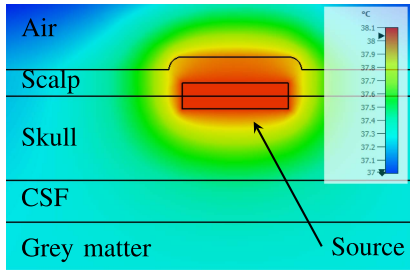

Fig. 7. Thermal simulation of the implanted receiver, generating 14.7 mW, performed in CST Studio Suite. The temperature ranges from 37.0 (blue) to 38.1 °C (red).

3) Tissue Heating by Heating of Components: According to EN-45502-1 [20] and ISO 14708-3 [21], the outer surface of any implantable neurostimulator should never exceed the surrounding body temperature by more than 2 °C.

The heat generated by the implanted receiver is equal to the dissipated power. For the current design, the computed losses are 14.6 mW for $k = k_{opt}$. The volume of the rectifier is $7.4 \times 6.4 \times 2.0$ mm^3, with a surface area of 150 mm^2. This corresponds to a maximum heat flux of 9.7 mW/cm^2.

A thermal simulation was performed in Simulia CST Studio Suite, similar to [41], using the thermal properties of human tissue from [40], listed in Table III. The thermal source was a perfect thermal conductor (PTC) volume with the same dimensions as the rectifier. The source is assumed to be on the skull-scalp boundary. A range of simulations was performed, with the scalp thickness varying from 2 to 4 mm, the skull thickness varying from 3 to 6.5 mm, and the CSF layer being 3.2 mm thick [30], [31], [32].

Fig. 7 shows the resulting temperature distribution for the worst-case scenario; a skull thickness of 6.5 mm, and a scalp thickness of 2 mm. The maximum temperature increase, compared to the case without an active thermal source, is 0.86 °C. As can be seen in the Figure, the scalp is assumed to warp around the implant, maintaining its thickness. If the outer surface of the scalp is assumed to stay flat, the resulting maximum temperature changes less than 0.01 °C.

The simulated receiver can dissipate 36.0 mW before the 2 °C limit is reached. This implies the prototype complies with ISO 14708-3, even in the worst case. In practice, an enclosure will be added to the rectifier, enlarging the surface area, hence lowering the heat flux, meaning that more energy can be dissipated before the 2 °C limit is reached.

The heat flux of the Rx coil is over 10 times lower than that of the rectifier. It thus complies with the standard.

VI. RESULTS

The prototype described in the previous Section is validated for $R_L = 544$, 700, and 980 Ω, corresponding to 90, 70, and 50 mW received power at $V_{out} = 7$ V, respectively. As the link is designed to deliver 90 mW, the efficiency will be given at $R_L =$

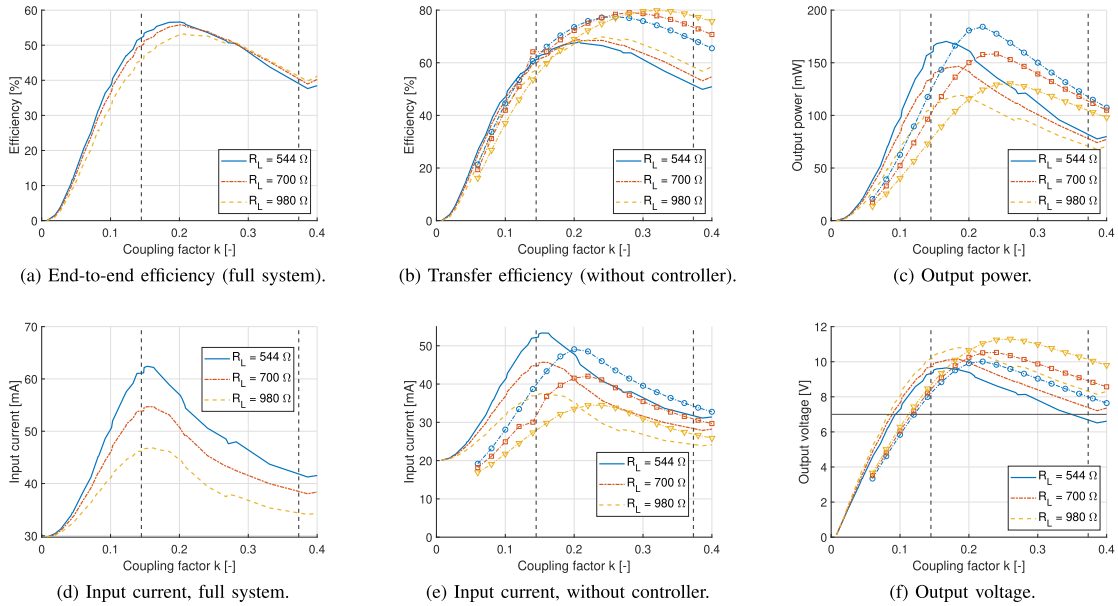

(a) End-to-end efficiency (full system). (b) Transfer efficiency (without controller). (c) Output power.

(d) Input current, full system. (e) Input current, without controller. (f) Output voltage.

Fig. 8. Simulated and measured efficiency, output power, input current, and output voltage of the manufactured prototype for $V_{in} = 5\,V$ and three different load resistances. Unmarked line = measured, marked line = simulated. $R_L = 544\,\Omega$ circular marker, $R_L = 700\,\Omega$ square marker, $R_L = 980\,\Omega$ triangular marker.

$544\,\Omega$. Fig. 8 shows the simulated and measured efficiency η, input current I_{dc}, and output voltage V_{out} and power P_{out}, as a function of the coupling factor k.

From Fig. 8, it can be observed that the shapes of the simulation and measurement curves are very similar, but the peak in output power and input current in the prototype occurs at a coupling factor around 0.05 lower than the simulations. Additional measurements have shown that the spice model of the MOSFET is inaccurate in terms of parasitics, and also that the parasitics of the three coils L_c, L_1, and L_2 are significant at 6.78 MHz. These observations could explain the shift in behavior. Furthermore, the coupling factor was measured with the Rx coil submerged in a 0.9% saline solution, which might have unintentionally influenced the result.

Fig. 8(c) shows that the prototype is able to deliver at least 80 mW power to the load for $8 \leq h \leq 15$ mm and $0 \leq d \leq 15$ mm. The end-to-end efficiency is between 39 and 57%.

In literature, the power consumption of the controller and gate driver are often ignored in the reported efficiency. The measured efficiency of the link without oscillator and gate driver, also referred to as the transfer efficiency, is between 52 and 68%. Up to 170 mW can be transferred when $k = 0.17$, with a transfer efficiency of 65%.

The mismatch in output voltage between the prototype and the simulation is up to 17%. However, when the measured curve is shifted by $\Delta k = 0.05$, as discussed above, the difference drops below 4%. In that case, the difference in input current is at most 8%.

VII. Conclusion

An approach for the design of a biomedical WPT system consisting of a class-E inverter, a class-DE rectifier, and two coupled coils, optimized for MPTE, was presented. The design was validated in a case study; circuit simulations were performed, and a prototype was manufactured. There is a good agreement between the simulations and the measurements, when a shift in coupling factor of $\Delta k = 0.05$ is taken into account. In that case, the difference in output voltage is below 4%, and the difference in input current is below 8%.

The WPT link designed for the case study can transfer over 80 mW at 7 V to a biomedical brain implant transcutaneously at 6.78 MHz. The end-to-end efficiency is between 39 and 57%. The transfer efficiency, where the controller and gate driver are ignored, is between 52 and 68%. Up to 170 mW can be transferred when $k = 0.17$, with a transfer efficiency of 65%.

The presented system complies with relevant (medical) standards IEEE Std C95.1, ICNIRP, ETSI EN 303 417, EN-45502-1, and ISO 14708-3 for distances between the coils of $8 \leq h \leq 15$ mm, and misalignment from $0 \leq d \leq 15$ mm.

VIII. Future Work

Future work can benefit from MOSFET and diode spice models that are more accurate at the relatively low power levels under consideration. Furthermore, the behavior of the Tx and Rx coils in the vicinity of human tissue should be further investigated. Additionally, the behavior of the feed inductor L_c should be more accurately determined for this specific application, where the current flowing through it is a combination of DC and AC.

References

[1] R. R. Bourne et al., "Trends in prevalence of blindness and distance and near vision impairment over 30 years: An analysis for the global burden of disease study," *Lancet Glob. Health*, vol. 9, no. 2, pp. e130–e143, 2021.

[2] X. Chen, F. Wang, E. Fernández, and P. R. Roelfsema, "Shape perception via a high-channel-count neuroprosthesis in monkey visual cortex," *Science*, vol. 370, no. 6521, pp. 1191–1196, 2020.

[3] NESTOR, "NESTOR - Neuronal stimulation for recovery of function," 2022. [Online]. Available: www.nestor-sight.com

[4] K. Agarwal, R. Jegadeesan, Y. X. Guo, and N. V. Thakor, "Wireless power transfer strategies for implantable bioelectronics," *IEEE Rev. Biomed. Eng.*, vol. 10, no. 3, pp. 136–161, Mar. 2017.
[5] G. L. Barbruni, P. M. Ros, D. Demarchi, S. Carrara, and D. Ghezzi, "Miniaturised wireless power transfer systems for neurostimulation: A. review," *IEEE Trans. Biomed. Circuits Syst.*, vol. 14, no. 6, pp. 1160–1178, Dec. 2020.
[6] M. J. Karimi, A. Schmid, and C. Dehollain, "Wireless power and data transmission for implanted devices via inductive links: A systematic review," *IEEE Sensors J.*, vol. 21, no. 6, pp. 7145–7161, Mar. 2021.
[7] S. Roy, A. N. M. W. Azad, S. Baidya, and F. Khan, "A comprehensive review on rectifiers, linear regulators, and switched-mode power processing techniques for biomedical sensors and implants utilizing in-body energy harvesting and external power delivery," *IEEE Trans. Power Electron.*, vol. 36, no. 11, pp. 12721–12745, Nov. 2021.
[8] G. A. Kendir et al., "An optimal design methodology for inductive power link with class-E amplifier," *IEEE Trans. Circuits Syst. I, Regular Papers*, vol. 52, no. 5, pp. 857–866, May 2005.
[9] D. Jiang, D. Cirmirakis, M. Schormans, T. A. Perkins, N. Donaldson, and A. Demosthenous, "An integrated passive phase-shift keying modulator for biomedical implants with power telemetry over a single inductive link," *IEEE Trans. Biomed. Circuits Syst.*, vol. 11, no. 1, pp. 64–77, Feb. 2017.
[10] M. W. Baker and R. Sarpeshkar, "Feedback analysis and design of RF power links for low-power bionic systems," *IEEE Trans. Biomed. Circuits Syst.*, vol. 1, no. 1, pp. 28–38, Mar. 2007.
[11] C. Liu, C. Jiang, J. Song, and K. T. Chau, "An effective sandwiched wireless power transfer system for charging implantable cardiac pacemaker," *IEEE Trans. Ind. Electron.*, vol. 66, no. 5, pp. 4108–4117, May 2019.
[12] Y. Park et al., "A frequency-splitting-based wireless power and data transfer IC for neural prostheses with simultaneous 115 mW power and 2.5 Mb/s forward data delivery," in *Proc. IEEE Int. Solid-State Circuits Conf.*, 2021, pp. 472–474.
[13] *IEEE Standard for Saf. Levels with Respect to Hum. Exposure to Electric, Magn., and Electromagn. Fields, 0 Hz to 300 GHz'*, Synopsis of IEEE Standard C95.1-2019, 2019.
[14] G. Ziegelberger et al., "ICNIRP guidelines for limiting exposure to electromagnetic fields (100 kHz to 300 GHz)," in *Proc. Int. Commission Non-Ionizing Radiat. Protection*, 2020, pp. 483–524.
[15] G. Sun, B. Muneer, Y. Li, and Q. Zhu, "Ultracompact implantable design with integrated wireless power transfer and RF transmission capabilities," *IEEE Trans. Biomed. Circuits Syst.*, vol. 12, no. 2, pp. 281–291, Apr. 2018.
[16] M. Yuan et al., "Magnetic resonance-based wireless power transfer for implantable biomedical microelectronics devices," in *Proc. IEEE Int. Symp. Signal Process. Inf. Technol.*, 2019, pp. 2019–2022.
[17] M. L. Navaii, H. Sadjedi, and A. Sarrafzadeh, "Efficient ASK data and power transmission by the class-E with a switchable tuned network," *IEEE Trans. Circuits Syst. I, Regular Papers*, vol. 65, no. 10, pp. 3255–3266, Oct. 2018.
[18] *Wireless Power Transmiss. Syst.; Harmonised Eur. Standard*, ETSI EN 303 417 V1.1.1, ETSI, Sophia Antipolis, France, 2017.
[19] C. Xiao, D. Cheng, and K. Wei, "An LCC-C compensated wireless charging system for implantable cardiac pacemakers: Theory, experiment, and safety evaluation," *IEEE Trans. Power Electron.*, vol. 33, no. 6, pp. 4894–4905, Jun. 2018.
[20] *Implants for Surg. - Act. Implantable Med. Devices; Eur. Standard*, EN-45502-1, 2015.
[21] *Implants for Surg. – Act. implantable Med. Devices – Part 3: Implantable Neurostimulators*, ISO 14708-3: 2018, 2008.
[22] X. Wei et al., "Nanofabricated ultraflexible electrode arrays for high-density intracortical recording," *Adv. Sci.*, vol. 5, no. 6, 2018, Art. no. 1700625.
[23] F. Shahrokhi, K. Abdelhalim, D. Serletis, P. L. Carlen, and R. Genov, "The 128-channel fully differential digital integrated neural recording and stimulation interface," *IEEE Trans. Biomed. Circuits Syst.*, vol. 4, no. 3, pp. 149–161, Jun. 2010.
[24] A. E. Omisakin, R. M. C. Mestrom, and M. J. Bentum, "Low-power wireless data transfer system for stimulation in an intracortical visual prosthesis," *Sensors (Switzerland)*, vol. 21, no. 3, pp. 1–16, 2021.
[25] S. U. Rehman, A. M. Kamboh, and Y. Yang, "A 79 μW 0.24mm2 8-channel neural signal recording front-end integrated circuit," in *Proc. Int. Conf. Appl. Electron.*, 2017, pp. 24–27.
[26] M. Pinuela, D. C. Yates, S. Lucyszyn, and P. D. Mitcheson, "Maximizing DC-to-load efficiency for inductive power transfer," *IEEE Trans. Power Electron.*, vol. 28, no. 5, pp. 2437–2447, May 2013.
[27] M. Kamon, J. K. White, and M. J. Tsuk, "FASTHENRY: A. multipole-accelerated 3-D inductance extraction program," *IEEE Trans. Microw. Theory Techn.*, vol. 42, no. 9, pp. 1750–1758, Sep. 1994.
[28] M. Dionigi, M. Mongiardo, and R. Perfetti, "Regorous network and full-wave electromagnetic modeling of wireless power transfer links," *IEEE Trans. Microw. Theory Techn.*, vol. 63, no. 1, pp. 65–75, Jan. 2015.
[29] U. M. Jow and M. Ghovanloo, "Modeling and optimization of printed spiral coils in air and muscle tissue environments," in *Proc. IEEE Conf. Eng. Med. Biol. Soc.*, 2009, vol. 3, no. 5, pp. 6387–6390.
[30] H. Hori, G. Moretti, A. Rebora, and F. Crovato, "The thickness of human scalp: Normal and bald," *J. Invest. Dermatol.*, vol. 58, no. 6, pp. 396–399, 1972.
[31] K. Wendel-Mitoraj, D. Stoliar, J. Malmivuo, and J. A. Hyttinen, "Measuring tissue thicknesses of the human head using centralized and normalized trajectories," in *Proc. Conf. Consciousness Measures*, 2009, pp. 112–113.
[32] P. Oltulu et al., "Measurement of epidermis, dermis, and total skin thicknesses from six different body regions with a new ethical histometric technique," *Turkish J. Plast. Surg.*, vol. 26, no. 2, pp. 56–61, 2018.
[33] A. Costanzo et al., "Conditions for a load-independent operating regime in resonant inductive WPT," *IEEE Trans. Microw. Theory Techn.*, vol. 65, no. 4, pp. 1066–1076, Apr. 2017.
[34] "LTspice simulator," 2022. [Online]. Available: www.analog.com/en/design-center/design-tools-and-calculators/ltspice-simulator.html
[35] T. van Nunen, R. Mestrom, and H. Visser, "Wireless power transfer to a visual prosthesis: 100 mW at 6.78 MHz," in *Proc. IEEE Int. Symp. Antennas Propag.*, 2021, pp. 269–270.
[36] M. K. Kazimierczuk and D. Czarkowski, *Resonant Power Converters*, 1st ed. New York, NY, USA: Wiley, 1995.
[37] K. Fukui and H. Koizumi, "Analysis of half-wave class DE low dv/dt rectifier at any duty ratio," *IEEE Trans. Power Electron.*, vol. 29, no. 1, pp. 234–245, Jan. 2014.
[38] T. Nagashima, X. Wei, E. Bou, E. Alarcon, and H. Sekiya, "Analytical design for resonant inductive coupling wireless power transfer system with class-E inverter and Class-DE rectifier," in *Proc. IEEE Int. Symp. Circuits Syst.*, 2015, pp. 686–689.
[39] S. Gabriel, R. W. Lau, and C. Gabriel, "The dielectric properties of biological tissues: III. parametric models for the dielectric spectrum of tissues," *Phys. Med. Biol*, vol. 41, pp. 2271–2293, 1996.
[40] G. Lazzi, "Thermal effects of bioimplants," *IEEE Eng. Med. Biol. Mag.*, vol. 24, no. 5, pp. 75–81, Sep.–Oct. 2005.
[41] S. Kim, R. A. Normann, R. Harrison, and F. Solzbacher, "Preliminary study of the thermal impact of a microelectrode array implanted in the brain," in *Proc. Annu. Int. Conf. IEEE Eng. Med. Biol. Soc.*, 2006, pp. 2986–2989.

Tom P. G. van Nunen (Student Member, IEEE) was raised in Deurne, The Netherlands. He received the M.Sc. degree from the Eindhoven University of Technology (TU/e), Eindhoven, The Netherlands, in 2017 on the topic of the influence of ambient temperature on the radiated emission of devices, measured in a reverberation chamber, and the Ph.D. degree from Electromagnetics Group, TU/e, in 2023. In 2018, he joined the Electromagnetics Group with the TU/e. He was a part of the NESTOR Project, which is developing a brain implant for blind people, with the aim to give them back a (crude) form of functional vision, together with other universities and institutes in The Netherlands and the USA. He was responsible for the wireless power transfer (WPT) to the implant. In 2023, he joined TNO, The Hague, The Netherlands, where he is working on electromagnetic effects.

Rob M. C. Mestrom (Member, IEEE) received the M.Sc. and Ph.D. degrees from the Mechanical Engineering Department, Eindhoven University of Technology (TU/e), Eindhoven, The Netherland, in 2005 and 2009, respectively. His Ph.D. work was on multiphysics modeling for microelectromechanical systems (MEMS). After a postdoc in the field of MEMS, RF antenna arrays and transceivers. Since 2012, he has been an Assistant Professor of the Electromagnetics Group of TU/e and a Researcher with the Electromagnetics for Care and Cure lab. His research interests include the application of electromagnetics to biomedical applications, which range from hyperthermia, antennas for wireless power transfer and communication, and phantom design. His interest relates to model-based personalization of (non-invasive) neurostimulation. He is on the Dutch Health Council to advise the Dutch government on electromagnetic fields and health-related queries.

Hubregt J. Visser (Senior Member, IEEE) received the M.Sc. degree in electrical engineering from Eindhoven University of Technology, Eindhoven, The Netherlands, in 1989, the Ph.D. degree from the Eindhoven University of Technology, and Katholieke Universiteit Leuven, Leuven, Belgium, in 2009. In 1990, after fulfilling his military service at TNO Physics and Electronics Laboratory, The Hague, The Netherlands, he joined the same laboratory as a civilian. He has participated in projects concerning near-field antenna measurements, monolithic microwave integrated circuits design, and phased-array antenna design. In 1996 to 1997, he was stationed at the European Space Research and Technology Centre, Noordwijk, The Netherlands, where he was on array antenna modeling. In 2001, he joined TNO Science and Industry, Eindhoven, working on antenna miniaturization. In 2009 he joined IMEC, Eindhoven, The Netherlands, where he is on Wireless Power Transfer. Since 2014, he has been a Full Professor with the Eindhoven University of Technology where he teaches antenna theory. He was Co-organizer and Co-Chair of the IEEE 2019 Wireless Power Week in London. He holds 12 patents, has written seven book chapters and author of the books *Array and Phased Array Antenna Basics* (Wiley, 2005), *Approximate Antenna Analysis for CAD* (Wiley, 2009) and *Antenna Theory and Applications* (Wiley, 2012).